Strain-driven broken twin boundary coherence in YBa$_2$Cu$_3$O$_{7-\delta}$ nanocomposite thin films

R. Guzman,[1] J. Gazquez,[1,2,a)] V. Rouco,[1] A. Palau,[1] C. Magen,[3] M. Varela,[2,4] J. Arbiol,[1,5] X. Obradors,[1] and T. Puig[1]

[1]*Institut de Ciencia de Materials de Barcelona, ICMAB-CSIC, Campus de la UAB, 08193 Bellaterra, Catalonia, Spain*
[2]*Materials Science and Technology Division, Oak Ridge National Laboratory, Oak Ridge, Tennessee 37831, USA*
[3]*Laboratorio de Microscopías Avanzadas, Instituto de Nanociencia de Aragon-ARAID and Departamento de Física de la Materia Condensada, Universidad de Zaragoza, 50018 Zaragoza, Spain*
[4]*Departamento de Física Aplicada III, Universidad Complutense de Madrid, 28040 Madrid, Spain*
[5]*Institucio Catalana de Recerca i Estudis Avançats (ICREA), 08010 Barcelona, Catalonia, Spain*

In this letter we use high resolution scanning transmission electron microscopy to study epitaxial YBa$_2$Cu$_3$O$_{7-\delta}$ (YBCO) nanocomposite thin films. We find that twin boundaries (TB) in YBCO nanocomposite thin films are disturbed by the presence of secondary phase nanoparticles as well as by intergrowths. Secondary phases promote the nucleation of TBs and, at the same time, result in bending, decreasing and changing the TB's spacing. On the other hand, the local strain ensuing from the partial dislocation associated to Y248 and Y125 intergrowths break the vertical coherence of TBs. This interaction results in a complex domain structure where twin boundary coherence is no longer satisfied and twin spacing is reduced down to a few nanometers precluding vortex channeling at low temperatures. © 2013 American Institute of Physics. [http://dx.doi.org/10.1063/1.4793749]

While high temperature superconductors (HTS) have reached high standards, there is still a strong interest in developing YBa$_2$Cu$_3$O$_{7-\delta}$ (YBCO)-based thin films and tapes with enhanced critical current densities for electronic and power applications[1,2] and plenty of room for improvement. A fundamental challenge is to immobilize the magnetic flux lines and thus prevent resistive losses in the presence of large magnetic fields. This problem can be tackled through nanoscale engineering of defects in the crystal. Vortex pinning is extremely dependent on the microstructure of the HTS films, and vortex interaction with defects is rather complex. For example, extended defects such as grain boundaries with misorientation angles greater than 5° might depress critical currents,[3,4] but they can also exhibit much higher critical current densities due to the presence of dislocations, twin boundaries, intergrowths, etc. These defects can pin the magnetic flux lines and promote an enhancement of the superconducting properties.

Unfortunately, the naturally occurring defects are not effective enough at large magnetic fields. Significant research has been directed at strategies based on nano-engineering of ordered arrays of defects, which have achieved effective flux pinning,[5–9] and recently even the possibility to suppress the pinning anisotropy in very high J$_c$ films.[10,11] The nanocomposite HTS films exhibit a challenging open front where a non-superconducting phase is dispersed in the superconducting matrix. By modifying the deposition technique, the formation of either coherent, cube-on-cube epitaxially oriented nanoparticles within the bulk of the film or incoherent, randomly oriented nanodots can be achieved.[7,8,11] The ensuing different microstructures render dramatic changes in the flux pinning mechanism: while films grown by pulsed laser deposition (PLD) show directional effects in J$_c$, solution derived composites exhibit a characteristic isotropic pinning behavior. The solution derived nanocomposites feature a huge increase of the Y$_2$Ba$_4$Cu$_8$O$_{16}$ (Y248) intergrowths, consisting of an extra Cu-O chain layer. These defects, along with twin boundaries (TB), are the most widespread defects and thus more relevant to the microstructure and critical currents of the YBCO films. It has been recently established that TBs may act both as pinning sites or flux channels depending on the temperature and the magnetic field orientation[12] and that Y248 intergrowths, specially the associated partial dislocations of their boundaries, also play a very important role in vortex pinning.[11,13,14]

In this scenario, the investigation of the atomic structure of individual defects, their intrinsic self-assembling behavior as well as their interaction is thus critical to the understanding of the flux pinning efficiency of the HTS nanocomposites. In the present letter, we use aberration corrected scanning transmission electron microscopy (STEM) to study TBs and Y248 planar defects in solution derived YBa$_2$Cu$_3$O$_{7-x}$-BaZrO$_3$ (YBCO-BZO) nanocomposite thin films. A standard four probe transport technique was used to measure the critical current density angular dependence, $J_c(\theta)$. The samples where rotated in a maximum Lorentz Force configuration, being θ the angle between the magnetic field and the crystallographic c-axis of the YBCO film. We will show how the embedded secondary phases act as extra nucleation centers for the formation of twin boundaries, resulting in films with higher density of twin domains and shorter twin spacing. Both nanoparticles and the associated defects distort the twin boundaries affecting both their spacing and coherence across the entire sample thickness. These defects yield changes in dimensionality, size,

---

a)Author to whom correspondence should be addressed. Electronic mail: jgazqueza@gmail.com.

and even orientation of the TBs, which will definitely affect their roles as pinning sites or as flux channels. In particular, it is shown that vortex channeling is strongly precluded in nanocomposites.

YBCO-BZO nanocomposite films with thicknesses in the 250 nm range were grown on (001) LaAlO$_3$ substrates. Samples were prepared from metalorganic precursor solutions with stoichiometric quantities of Y, Ba, and Cu anhydrous trifluoroacetates, where Ba or Zr anhydrous trifluoroacetates have been added to achieve the desired composition of the YBCO-BZO nanocomposites, in this case 10% molar. Further details on solution preparation, deposition, and processing can be found in previous works.[11,15–17] These settings result in a superconducting YBCO layer with high values of isotropic pinning force, $F_p^{max} \sim 20 \, GN \, m^{-3}$ (10 mol. % BZO).[10] X-ray diffraction analysis showed (001)-oriented YBCO films with a typical rocking curve width of the (005) peak $<0.5°$ and in-plane orientation spread $<1°$, indicating very good crystallographic alignment.

Cross-sectional and plan-view nanocomposite specimens were investigated by conventional transmission electron microscopy (TEM) and aberration corrected STEM. Bright-field TEM experiments were carried out in a JEOL 2010F field-emission gun microscope. High-resolution high-angle annular dark-field (HAADF) STEM studies were performed in a Nion UltraSTEM, operated at 100 kV and equipped with a Nion aberration corrector, and in a FEI Titan (60–300 kV) equipped with a probe-aberration corrector, a monochromator, and a X-FEG electron gun. The HAADF detector allows recording incoherent Z-contrast images, in which the intensity of atom columns directly reflects their mean square atomic number (Z).[18] Specimens for STEM and conventional TEM were prepared by conventional methods, by grinding, dimpling and Ar ion milling.

Figure 1(a) shows a plan-view bright-field TEM image of the film taken near the [001] zone axis with (110) as the diffraction vector, g = (110). YBCO twin domains are shaped in the form of lamellae parallel to their TBs and appear in order to relieve the spontaneous strain that arises during the tetragonal-to-orthorhombic transition that takes place during the oxygenation step.[19,20] Figure 1(a) shows a single domain of TBs (yellow arrows), along with several

secondary phase nanoparticles (dashed lines). The areas featuring strong diffraction contrast might correspond to Y248 planar defects, as expected for such diffraction conditions;[21,22] however, the highly distorted YBCO matrix of these nanocomposites hinders the identification of isolated defects. Certainly, a cross-sectional view of a YBCO nanocomposite thin film (see Figure 1(b)) shows a high density of Y248 planar defects, higher than what it is typically observed in YBCO-TFA films grown by chemical solution deposition (CSD)[23] (see also supplementary material[24]). The Y248 planar defects appear as dark stripes in the Z-contrast image and are found to be intimately connected to the generation of incoherent interfaces between the YBCO epitaxial matrix and the non-superconducting phase.[11] Figure 1 shows a clear example of how the TBs are disturbed by the presence of the BZO nanoparticles. The most obvious change is the variation of the TB spacing and the bowing of the boundary walls.

A higher resolution image reveals these changes in detail. Figure 2(a) depicts a plan-view high resolution Z-contrast image with a BZO nanoparticle embedded within the YBCO matrix. Careful inspection of the YBCO lattice unveils the rotation of the atomic planes across the TBs and allows their delimitation, as shown in the inset. Geometrical phase analysis (GPA) software[25] helps processing the whole image and characterizing the domain map. This software is based on the Fourier analysis of a high resolution lattice image selecting a strong Bragg reflection and performing an inverse Fourier transform. The phase component of the resulting complex image gives information on local displacements and rotations of atomic planes. Figure 2(b) shows a map of Figure 2(a) calculated with the GPA software: a plot of the fringe rotation map of the {110}$_{YBCO}$ selected Bragg reflection. The change in color from red to green shows the rotation (in degrees) of the lattice fringes. Because the selected Bragg reflection belongs to YBCO planes, a calculation artifact appears within the region delimited by the BZO nanoparticle. The calculated value of the angle between adjacent twins along the ⟨110⟩ direction perfectly matches with
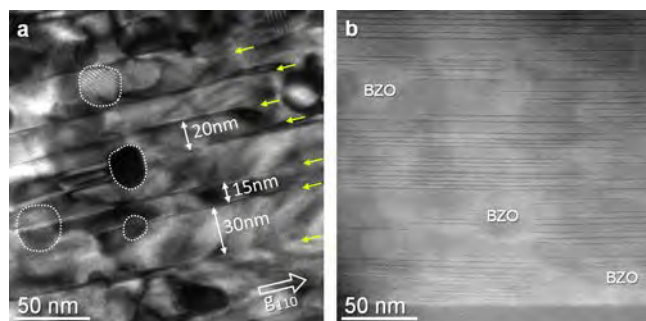
FIG. 1. (a) Bright field TEM micrograph under two beam condition with g = 110. Under these diffraction conditions TBs appear as dark stripes (yellow arrows point to TBs in the image). Randomly distributed nanoparticles are observed (marked with dashed lines in the image). (b) Cross-sectional low magnification Z-contrast image of a nanocomposite with BZO nanoparticles embedded within the YBCO matrix. Dark horizontal stripes correspond to Y248 intergrowths.
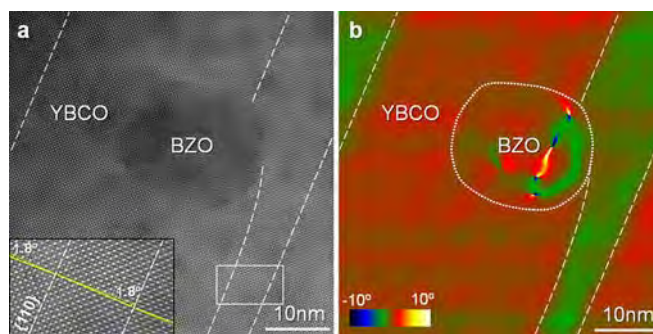
FIG. 2. (a) Plan-view high resolution Z-contrast image of a 20 nm embedded BZO nanodot within the YBCO matrix viewed along the [001] zone axis. Along this zone axis, the brightest spots represent the heavy Y/Ba columns, while the lighter Cu columns appear dimmer. The inset shows a magnified image of the squared region where the change in orientation of the lattice planes while crossing the boundaries is observed. (b) Fringe rotation map corresponding to image (a) of the {110}$_{YBCO}$ lattice planes showing the rotation (in degrees) of lattice fringes between adjacent twins. Twin spacing changes due to the nanoparticle presence. Colors show different rotation angles. {110} YBCO Bragg reflections were used to generate the fringe rotation map, which cause an artifact within the nanoparticle region.
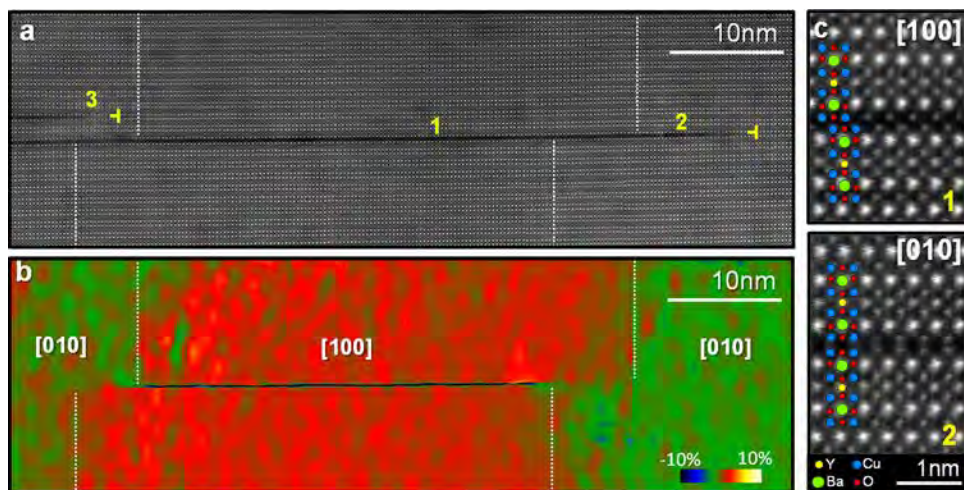
FIG. 3. (a) A composition of consecutive atomic resolution Z-contrast images along a particular Y248 planar defect of a YBCO nanocomposite cross-sectional specimen. (b) e_{xx} deformation map showing in colors (red and green) different deformation values. Region 3 in (a) was taken as a reference area. (c) Close up views of regions 1 and 2 labeled in (a) corresponding to two sides of a twin boundary, which permits determination of the [010] and [100] zone axes in (b). The brightest spots correspond to Ba columns, followed by Y and finally by Cu, being the darkest contrast shown by the atomic planes containing Cu-O chains.

the theoretical value obtained from the orthorhombic cell, i.e., 1.78°. On the left side of the image a sharp and straight boundary is observed, whereas the following TB is strongly perturbed by the presence of a BZO nanodot. Here again, it is observed that TB spacing changes due the presence of the BZO nanoparticle, being reduced to a few nanometers.

As mentioned before, the solution derived YBCO nanocomposites are characterized by a high concentration of randomly distributed nanoparticles, resulting in a high density of Y248 planar defects. An isolated Y248 intergrowth with a finite lateral length is structurally analogous to a Frank loop, i.e., an extrinsic stacking fault surrounded by a partial dislocation. It is clear then that a high density of intergrowths will distort the YBCO matrix[11] and might affect the TB as well. Cross-sectional views permit a better visualization of the TB-Y248 intergrowth interaction. Figure 3(a) shows a high resolution Z-contrast image of the YBCO lattice in the presence of a Y248 intergrowth. The Y248 intergrowth involves a shift of half the unit cell along the b_{YBCO} axis; hence, one can easily identify different zone axes across the TB, as it is clearly seen in Figure 3(c), which shows two enlarged images corresponding to regions 1 and 2 of Figure 3(a), identified as [010] and [100] zone axes, respectively. Just like in the planar view, the GPA software helps mapping the twin boundaries, in this case calculating the e_{xx} deformation tensor, though. [100] and [010] domains can be unambiguously distinguished by GPA due to the existing differences between a and b cell parameters in the YBCO orthorhombic phase ($a = 0.382$ nm; $b = 0.388$ nm). Figure 3(b) shows the e_{xx} deformation tensor map ensuing from the {100} Bragg reflection, where the [100] and [010] domains are depicted as red and green, respectively. The dark horizontal fringe observed in the center of the map in Figure 3(c) is the result of the region where the periodicity of $(100)_{YBCO}$ planes is truncated due the shift along b. On the other hand the Y248 defect appears invisible in the green colored areas because there is no $^1/_2b$ shift of the Y248 structure along the [100] crystalline direction. As shown in Figure 3(a), the interaction of the TBs with the Y248 is likely to be strain-mediated. The stress built up due to an extra Y248 intergrowth and the ensuing local stress from its partial dislocation constitutes a strain barrier for the TB growth front propagation, see regions 2 and 3 in the image. It is also worth noting that this

image corresponds to an almost defect-free region of the sample and although the TB coherence is broken, its spacing is close to the one observed in standard YBCO films, ∼45 nm (see supplementary material[24]). On the other hand, in heavily faulted regions it is observed that the TB spacing is shortened mightily (≤10 nm).

Figure 4 shows an enlarged region of a BZO/YBCO interface. It is clear that in this region the YBCO matrix is strongly distorted and the (00l) planes are bent due to the presence of numerous intergrowths. A careful inspection of the micrograph permits probing, cell by cell, the successive changes of the YBCO basal axes. For the sake of clarity, different colors represent different domains in the image. A patchwork-like pattern is observed as a result of broken twin coherence and different twin spacing.

Since the orthorhombic phase exhibits a higher O content than the tetragonal phase, {110} twin domain formation
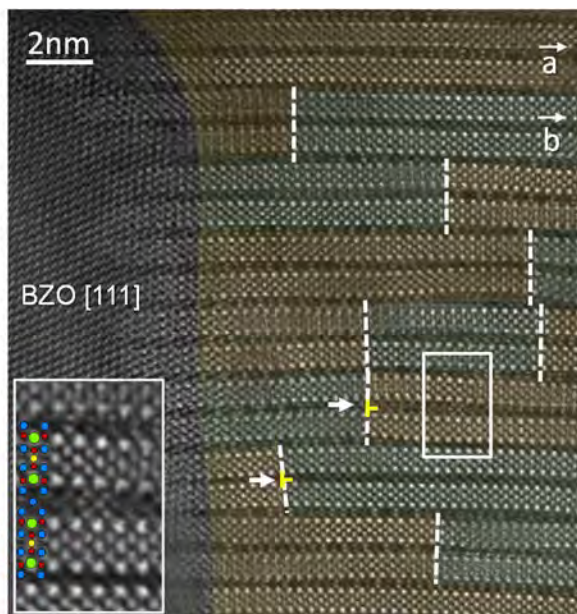

FIG. 4. High resolution Z-contrast image showing a YBCO/BZO interface. Green and brown colored regions mark different twin domains, where green corresponds to [100] YBCO zone axis orientation and brown to [010] zone axis. The arrows point to local intergrowths with one and two extra Cu-O chains added to the YBCO structure. The inset shows a triple chain intergrowth, $YBa_2Cu_5O_8$ (Y125).

is strongly determined by O diffusion within the film during the phase transformation process, and consequently, by the microstructure of the sample. In a defect-free environment, the formation of coherent twins in YBCO results from the heterogeneous nucleation of oxygen-rich centers of the orthorhombic phase at the surface of the grains (at grain boundaries and pores). Afterwards, the nuclei grow and extend deeper into the grain by incorporating oxygen supplied from ambient through the pore-grain boundary-twin boundary network and by incorporating twin nuclei that might have been eventually formed inside the grain. During the last stage of twin formation coarsening takes place, eliminating some of the twin boundaries and thus decreasing total free energy.[20] In the case of the present YBCO epitaxial nanocomposites, the interfaces between the superconductor and the secondary phase nanoparticles are expected to constitute additional nucleation sites for twin boundaries due to the broken symmetry, strain, and altered chemical structure, which decrease the nucleation barrier. In addition, defects in highly faulted films, like the ones studied here, constitute additional paths for O transport.[26,27] As observed in Figure 1(b), YBCO nanocomposite films feature plenty of randomly staggered Y248 defects. As previously reported, these planar defects have a marked irregular shape which stacking leads to highly strained three-dimensional regions within the YBCO lattice.[11] These highly localized and strained regions might pin the twin boundaries; thus, the final domain pattern will be a consequence of the TB-planar defects interaction. TBs must adapt to lattice distortions and strain barriers associated to Y248 defects and their associated partial dislocations. A paradigmatic example is shown in Figure 4. The arrows point to local intergrowths with one and even two extra Cu-O chains added to the YBCO structure, the later corresponds to a local composition of $YBa_2Cu_5O_8$ (Y125) and it is shown in detail in the inset. Y125 intergrowths are shorter in length (few nanometers), and the higher local strain generated prevents the advance of adjacent twin boundaries. As observed in Figure 3, Y248 and Y125 partial dislocations appear to pin the propagation of TBs. This interaction results in a scenario where twin boundaries are no longer coherent along the twin domain, being sometimes the twin spacing reduced down to few nanometers (see Figure 4). Indeed, in such faulted regions the twin boundary coherence along the c-axis could be as small as just one Y248 unite cell.

The effect of nanoparticles and the associated defects onto vortex pinning has been evaluated from the J_c angular dependence of a standard YBCO film (without BZO nanoparticles) and a YBCO-BZO nanocomposite. In Figures 5(a) and 5(b) we plot $J_c(\theta)$ measured at $\mu_0 H = 9$T and at two different temperatures, $T = 10$ K and 65 K, respectively, for both samples. Solid lines correspond to the isotropic pinning contribution determined by means of the Blatter scaling approach.[28] It should be noted that the incorporation of BZO nanoparticles produce a clear enhancement of the isotropic J_c contribution associated to the highly nanostrained YBCO matrix induced in the nanocomposites.[11] In addition, the contribution of anisotropic pinning defects (intergrowths and twin boundaries) can be evaluated by subtracting the isotropic contribution from the total $J_c(\theta)$ at the θ value where
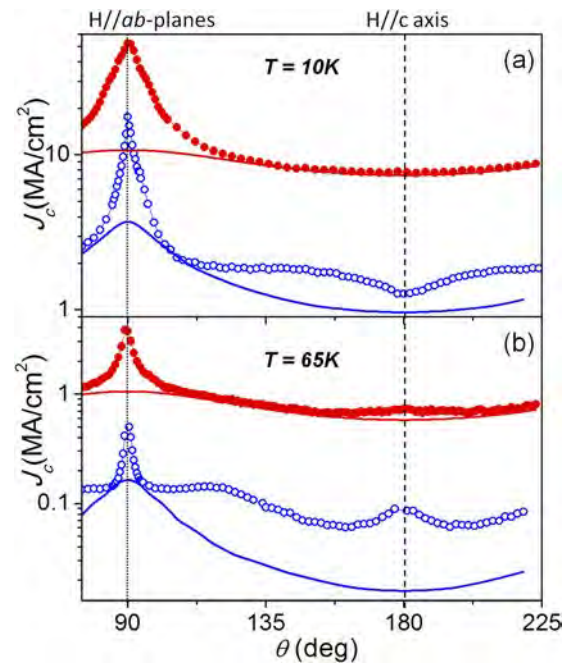

FIG. 5. Angular dependence of J_c at 9T, for a standard YBCO film (open symbols) and a nanocomposite (closed symbols) at (a) 10 K and (b) 65 K. Solid lines correspond to the J_c random pinning contribution determined using the Blatter scaling approach. Dotted and dashed lines mark the orientation of magnetic field direction along the **ab** planes and c axis, respectively.

the magnetic field is oriented along the anisotropic defect. Thus, pinning associated to anisotropic extended defects parallel to the *ab* planes, such as Y248 and Y125 intergrowths, can be estimated by analysing the width of the J_c peak appearing above the isotropic J_c contribution when H is aligned parallel to the *ab*-planes (dotted line in Fig. 5 at $\theta = 90°$). The full width at half maximum values obtained for the standard sample at 65 K and 10 K are 2.5° and 4.6°, respectively. Instead, for the nanocomposite much larger values have been found, i.e., 4.0° at 65 K and 11.4° at 10 K, evidencing the effect of a higher density of intergrowths.

Regarding the effect of twin boundary distribution on vortex pinning, we must evaluate the anisotropic J_c contribution when H is aligned along the c-axis (dashed line in Fig. 5 at $\theta = 180°$). At this θ value a J_c peak over the isotropic contribution is observed in the $J_c(\theta)$ curves measured at 65 K for both samples (dashed line in Figure 5(b)) indicating that there is a pinning contribution of c-axis correlated defects (mainly twin boundaries) to the total J_c. A quantification of this anisotropic contribution can be performed by subtracting the isotropic $J_c(\theta)$ (solid lines in Figure 5) from the experimental J_c curve (symbols in Figure 5). By doing that on a standard sample, we obtain that at $\theta = 0°$ and 65 K a 84% of J_c comes from c-axis anisotropic pinning defects (twin boundaries) whereas for the nanocomposite and due to their nearly isotropic pinning performance, the fraction of pinning force associated to twin boundaries is just 21%. On the other hand, we have demonstrated that the main effect of BZO nanoparticles on the TB distribution is the reduction of their vertical coherence along the c-axis. This lack of coherence should also have a significant effect on the J_c performance at low temperatures where vortices easily channel along TBs.[12] Indeed $J_c(\theta)$ curves measured for a standard sample and

YBCO-BZO nanocomposite at low temperature, 10 K (Figure 5(a)), show that the standard sample presents a sharp suppression of J_c at $\theta = 0$ K (dashed line in Figure 5(a)) associated to easy vortex sliding along the TB planes (vortex channeling) whereas no hints of channeling are observed for the YBCO-BZO nanocomposite.

In conclusion, we have shown how TBs in YBCO nanocomposite thin films are disturbed by the presence of secondary phase nanoparticles as well as by intergrowths. Secondary phases promote the nucleation of TBs and, at the same time, result in bending, decreasing, and changing the TB's spacing. On the other hand, the local strain ensuing from the partial dislocation associated to Y248 and Y125 intergrowths break the vertical coherence of TBs. Since the shape, dimensionality, size, and orientation of defects are key parameters to define their relevance as flux pinning sites, this new scenario should definitely modify understanding of TBs in nanocomposites, acting as pinning sites or as flux channels. We show that the anisotropic pinning contribution coming from TBs (at high temperatures) has a minor role compared with the huge enhancement of isotropic pinning in nanocomposites. On the contrary, we demonstrate that the reduction of the TB vertical coherence has a relevant effect on precluding vortex channeling at low temperatures and thus avoiding a J_c suppression for field parallel to the c-axis.

[1]D. Larbalestier, A. Gurevich, D. M. Feldmann, and A. Polyanskii, Nature (London) **414**(6861), 368–377 (2001).
[2]A. Usoskin, J. Dzick, A. Issaev, J. Knoke, F. Garcia-Moreno, K. Sturm, and H. C. Freyhardt, Supercond. Sci. Technol. **14**(9), 676–679 (2001).
[3]D. Dimos, P. Chaudhari, and J. Mannhart, Phys. Rev. B **41**(7), 4038–4049 (1990).
[4]D. Dimos, P. Chaudhari, J. Mannhart, and F. K. Legoues, Phys. Rev. Lett. **61**(2), 219–222 (1988).
[5]S. R. Foltyn, L. Civale, J. L. Macmanus-Driscoll, Q. X. Jia, B. Maiorov, H. Wang, and M. Maley, Nat. Mater. **6**(9), 631–642 (2007).
[6]S. Kang, A. Goyal, J. Li, A. A. Gapud, P. M. Martin, L. Heatherly, J. R. Thompson, D. K. Christen, F. A. List, M. Paranthaman, and D. F. Lee, Science **311**(5769), 1911–1914 (2006).
[7]A. Goyal, S. Kang, K. J. Leonard, P. M. Martin, A. A. Gapud, M. Varela, M. Paranthaman, A. O. Ijaduola, E. D. Specht, J. R. Thompson, D. K. Christen, S. J. Pennycook, and F. A. List, Supercond. Sci. Technol. **18**(11), 1533–1538 (2005).
[8]K. Matsumoto and P. Mele, Supercond. Sci. Technol. **23**(1), 014001 (2010).
[9]C. Cantoni, Y. F. Gao, S. H. Wee, E. D. Specht, J. Gazquez, J. Y. Meng, S. J. Pennycook, and A. Goyal, ACS Nano **5**(6), 4783–4789 (2011).
[10]J. Gutiérrez, A. Llordes, J. Gazquez, M. Gibert, N. Roma, S. Ricart, A. Pomar, F. Sandiumenge, N. Mestres, T. Puig, and X. Obradors, Nat. Mater. **6**(5), 367–373 (2007).
[11]A. Llordés, A. Palau, J. Gázquez, M. Coll, R. Vlad, A. Pomar, J. Arbiol, R. Guzmán, S. Ye, V. Rouco, F. Sandiumenge, S. Ricart, T. Puig, M. Varela, D. Chateigner, J. Vanacken, J. Gutiérrez, V. Moshchalkov, G. Deutscher, C. Magen, and X. Obradors, Nat. Mater. **11**, 329–336 (2012).
[12]A. Palau, J. H. Durrell, J. L. MacManus-Driscoll, S. Harrington, T. Puig, F. Sandiumenge, X. Obradors, and M. G. Blamire, Phys. Rev. Lett. **97**(25), 257002 (2006).
[13]J. Gutiérrez, B. Maiorov, T. Puig, J. Gazquez, N. Roma, H. Wang, F. Sandiumenge, and X. Obradors, Supercond. Sci. Technol. **22**(1), 015022 (2009).
[14]T. G. Holesinger, L. Civale, B. Maiorov, D. M. Feldmann, J. Y. Coulter, J. Miller, V. A. Maroni, Z. J. Chen, D. C. Larbalestier, R. Feenstra, X. P. Li, M. B. Huang, T. Kodenkandath, W. Zhang, M. W. Rupich, and A. P. Malozemoff, Adv. Mater. **20**(3), 391–407 (2008).
[15]T. Puig, J. C. Gonzalez, A. Pomar, N. Mestres, O. Castano, M. Coll, J. Gazquez, F. Sandiumenge, S. Pinol, and X. Obradors, Supercond. Sci. Technol. **18**(8), 1141–1150 (2005).
[16]K. Zalamova, N. Roma, A. Pomar, S. Morlens, T. Puig, J. Gazquez, A. E. Carrillo, F. Sandiumenge, S. Ricart, N. Mestres, and X. Obradors, Chem. Mater. **18**(25), 5897–5906 (2006).
[17]X. Obradors, T. Puig, S. Ricart, M. Coll, J. Gazquez, A. Palau, and X. Granados, Supercond. Sci. Technol. **25**(12), 123001 (2012).
[18]S. J. Pennycook and D. E. Jesson, Ultramicroscopy **37**(1-4), 14–38 (1991).
[19]E. D. Specht, C. J. Sparks, A. G. Dhere, J. Brynestad, O. B. Cavin, D. M. Kroeger, and H. A. Oye, Phys. Rev. B **37**(13), 7426–7434 (1988).
[20]C. J. Jou and J. Washburn, J. Mater. Res. **4**(4), 795–801 (1989).
[21]J. Plain, T. Puig, F. Sandiumenge, X. Obradors, and J. Rabier, Phys. Rev. B **65**(10), 104526 (2002).
[22]J. Tafto, M. Suenaga, and R. L. Sabatini, Appl. Phys. Lett. **52**(8), 667–668 (1988).
[23]J. Gazquez, M. Coll, N. Roma, F. Sandiumenge, T. Puig, and X. Obradors, Supercond. Sci. Technol. **25**, 065009 (2012).
[24]See supplementary material at http://dx.doi.org/10.1063/1.4793749 for further information on the microstructure of standard and nanocomposite solution derived YBCO thin films.
[25]M. J. Hytch, E. Snoeck, and R. Kilaas, Ultramicroscopy **74**(3), 131–146 (1998).
[26]D. Muller and H. C. Freyhardt, Philos. Mag. Lett. **73**(2), 63–70 (1996).
[27]S. K. Chen, L. Zhou, K. G. Wang, X. Z. Wu, P. X. Zhang, and Y. Feng, Physica C **377**(4), 571–577 (2002).
[28]T. Puig, J. Gutiérrez, A. Pomar, A. Llordes, J. Gazquez, S. Ricart, F. Sandiumenge, and X. Obradors, Supercond. Sci. Technol. **21**(3), 034008 (2008).

Strain-driven broken twin boundary coherence in YBa2Cu3O7−δ nanocomposite thin films

R. Guzman, J. Gazquez, V. Rouco, A. Palau, C. Magen et al.

Additional information on Appl. Phys. Lett.